energies

MDPI

Article

Corrosion and Erosion Risks in Biomass–Coal Cofiring Boilers: A CFD-Based Safety Assessment of a 660 MW Tangentially Fired Boiler

Yuqiu Tian [1,2], Xiaomeng Xu [1,2,*], Lingjie Zhu [3,*], Lei Zhang [4,5], Qiang Wang [1,2] and Zhian Li [1,2]

1 College of Energy Environment and Safety Engineering, China Jiliang University, Hangzhou 310018, China
2 Zhejiang Key Laboratory of Industrial Carbon Metrology Technology, Hangzhou 310018, China
3 School of Engineering and Technology, China University of Geosciences, Beijing 100083, China
4 Henan Boiler and Pressure Vessel Inspection Technology Research Institute, Zhengzhou 450016, China
5 School of Resources and Environmental Engineering, Wuhan University of Science and Technology, Wuhan 430081, China
* Correspondence: xiaomeng.xu@cjlu.edu.cn (X.X.); zlj.cjlu@foxmail.com (L.Z.)

Abstract

Achieving the co-combustion of biomass and coal in utility boilers while reducing carbon dioxide emissions poses significant challenges owing to the divergent physicochemical properties of the fuels. These differences can induce high-temperature corrosion and erosion of heating surfaces, threatening boiler safety. Despite this, integrated CFD-based assessments of sulfidic corrosion and particle erosion risks remain insufficiently addressed under realistic biomass–coal cofiring conditions. In this study, an integrated CFD-based risk assessment framework was established for biomass–coal cofiring boilers. The main novelty lies in the combined evaluation of high-temperature sulfidic corrosion and particle erosion risks under different biomass injection strategies. Specifically, user-defined functions were developed to classify high-temperature sulfidic corrosion risks based on local O_2, CO, and H_2S concentrations; the effects of biomass injection layers were quantitatively compared; the Oka erosion model was coupled with CFD particle tracking to predict wall wear; and an entropy-weighted multi-indicator method was used to rank the overall safety of different cofiring strategies. This study found that sufficiently high near-wall H_2S concentrations in the main combustion zone indicate an increased risk of sulfidic corrosion under reducing-atmosphere conditions. Compared with pure coal combustion, biomass injection through layer A exacerbates wall corrosion, whereas biomass injection through layer AB mitigates it. Erosion is primarily localized near burner nozzles. Notably, biomass cofiring reduces the average erosion rate by 7.9–30.2% but increases the local maximum erosion rate by 7.1–25.1%. The comprehensive evaluation indicates that the condition with 30% RS injected from layer AB, mixed with coal, yields the best overall performance. The corrosion assessment is limited to sulfidic corrosion risks associated with reducing atmospheres and does not explicitly model alkali- or chlorine-induced corrosion. This study provides a theoretical foundation for biomass cofiring optimization and offers practical guidance for boiler operational safety and maintenance.

Keywords: biomass cofiring; erosion wear; high-temperature corrosion; numerical simulation; safety assessment

Academic Editor: Fernando Rubiera González

Received: 23 April 2026
Revised: 12 June 2026
Accepted: 25 June 2026
Published: 29 June 2026

Copyright: © 2026 by the author. Licensee MDPI, Basel, Switzerland. This article is an open access article distributed under the terms and conditions of the Creative Commons Attribution (CC BY) license.

1. Introduction

Biomass cofiring has been widely recognized for its considerable carbon neutrality benefits, and it offers an effective solution for the low-carbon transformation of coal-fired power plants [1,2]. This technology substantially reduces carbon dioxide emissions and pollutants (e.g., SO_x and NO_x) from coal-fired boilers [3–7] based on the co-combustion of biomass fuel and conventional fossil fuels at specific blending ratios. In addition, it facilitates the resource utilization of agricultural and forestry residues, generating both environmental and economic benefits. However, the cofiring process alters the temperature and velocity fields within the furnace owing to the notable differences in the combustion characteristics of biomass and coal, leading to a synergistic corrosion–erosion effect that adversely affects the operational efficiency and reliability of the boiler system [8,9]. Therefore, the corrosion and erosion characteristics of biomass and coal during cofiring, along with the optimization of their blending ratios, must be investigated in depth to ensure safe operation of utility boilers and facilitate the transition of energy production modes.

The impacts of biomass cofiring on high-temperature corrosion in coal-fired boilers have been extensively investigated [10–12]. Alkali metals and chlorine in biomass fuels have been shown to form low-melting-point eutectics and complex compounds during combustion, leading to the corrosion of boiler heating surfaces [13,14]. Vlček et al. [15] examined the effects of alkali-induced corrosion on the service life of boiler refractory materials during biomass combustion. Wang et al. [16] studied the corrosion mechanisms resulting from the co-combustion of coal and biomass. To address these issues, high-temperature corrosion mitigation methods have been proposed. For instance, Yuan et al. [17] developed a novel H_2S corrosion model to predict metal wastage in water-cooled walls. However, their model did not account for the cumulative effects of corrosion depth under varying operating conditions. Cao et al. [18] investigated the influence of secondary air vent swing angles and burner aspect ratios on water-wall corrosion in a 1000-MW tangential-fired boiler; yet, they overlooked internal flow field variations under different operational scenarios. Although these studies provide a valuable foundation for understanding high-temperature corrosion mechanisms, they mostly focus on specific fuel and boiler material combinations, failing to fully consider the multifaceted effects of different fuel blends, combustion conditions, and atmospheric variations on the corrosion process. Moreover, existing research predominantly relied on short-term or small-scale experiments, with limited knowledge on corrosion classification and simulation-based prediction of corrosion distribution across different boiler regions.

The erosion characteristics of boiler heating surfaces have been investigated through experimental and numerical approaches [19–21]. The boiler type significantly influences the combustion mode, particle dynamics, and gas–solid flow structure, leading to distinct erosion behaviors. In the context of circulating fluidized bed boilers, Vinod et al. [22] experimentally examined the erosion resistance of Superco-605-coated surfaces. Orumbayev et al. [23] obtained quantitative data on wear reduction in transverse finned tube bundles and tubular air heaters with different geometries. For pulverized coal boilers, Wu et al. [24] studied the erosion behavior of tube walls under varying impact velocities, temperatures, and attack angles using a high-temperature erosion testing apparatus. Saarivirta et al. [25] compared the erosion performance of various boiler steels under different operating conditions. However, while existing studies focused on the experimental investigations of the erosive effects of solid particles on boiler walls, numerical studies on erosion characteristics under cofiring conditions have remained relatively rare. Furthermore, existing numerical simulations remained limited in terms of the selection and applicability of erosion models, failing to adequately account for multifactor interactions under complex combustion conditions.

To the authors' knowledge, no previous study has simultaneously coupled CFD-based flue gas species prediction, wall-atmosphere corrosion classification, Oka erosion modeling, and entropy-based safety ranking under different biomass injection strategies in a full-scale tangentially fired boiler. To bridge this gap and address these limitations, this study systematically investigated the temperature field distribution and flue gas composition evolution during biomass–coal co-combustion and their impacts on boiler safety. This work contributes by: (1) developing a CFD-based corrosion-risk classification method using O_2, CO, and H_2S distributions; (2) applying the Oka erosion model to quantify wall wear under biomass–coal cofiring; (3) integrating corrosion and erosion indicators through an entropy-weighted safety assessment. The findings provide a theoretical basis for safe and efficient operation of biomass–coal cofiring boilers and offer practical guidance for mitigating corrosion and erosion.

2. Mathematical Models and Methods

2.1. Research Methodology

To establish a clear methodological framework and provide an overview of the evaluation procedures, a comprehensive research workflow of this study is presented before detailing the physical configuration of the studied system. The methodology systematically integrates the following sequential components: (1) establishment of the physical boiler geometry and corresponding mesh generation; (2) formulation of multi-phase physical models coupled with specific operating conditions tailored for biomass–coal co-firing; (3) rigorous model validation against empirical or design benchmarks; (4) quantitative evaluations of high-temperature corrosion via wall-atmosphere risk classification and erosion via discrete particle tracking; and (5) a comprehensive safety assessment and strategy ranking employing an entropy-weighted multi-indicator model. Each component is elaborated in detail in the following subsections.

This study investigated a 660-MW supercritical tangential-fired coal-fired boiler, with the schematic structure shown in Figure 1. The furnace dimensions were as follows: a height of 56.25 m, a width of 19.58 m, and a depth of 16.44 m. The burner system featured a symmetric arrangement of air inlets, including six primary air levels (denoted as A–F), seven secondary air levels (labeled AA, AB, BC, CD, DE, EF, and FF), and two separated over-fire air (SOFA) levels (SOFA1 and SOFA2).

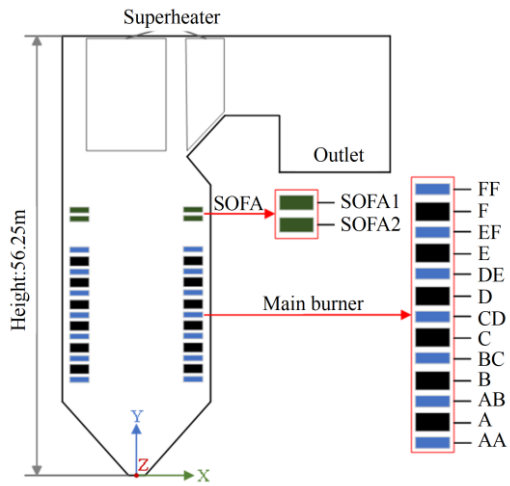

Figure 1. Schematic configuration of the boiler.

2.2. Mesh Generation

The complex gas–solid two-phase flow and chemical reactions within the boiler significantly influence the distribution of chemical species. These processes were simulated using ANSYS Fluent (2024 R2). The computational domain was partitioned into three distinct regions—the cold hopper, the main combustion zone, and the flue gas outlet section—with interface boundaries enabling data exchange between them [26]. A hexahedral structured mesh was adopted in accordance with the geometric features of the tangential-firing boiler. A coarser mesh was applied in these areas, considering relatively smooth parameter variations in the cold hopper and outlet regions. In contrast, the main combustion zone, characterized by intense reactions and steep velocity and temperature gradients, was discretized using a refined mesh. A grid independence study was conducted to evaluate the influence of mesh resolution on accuracy and efficiency. The comparison of simulation results for mesh sizes of 1.05×10^6, 2.42×10^6, and 3.69×10^6 cells under the BMCR condition is quantitatively summarized in Table 1, focusing on critical parameters at the boiler outlet (average temperature, NO_x concentration, and average velocity). As the mesh was refined from 2.42×10^6 to 3.69×10^6 cells, the relative variations for all monitored parameters were below 1.0%, demonstrating that further refinement had no significant effect [27]. Therefore, a mesh consisting of approximately 2.42×10^6 cells was selected for all subsequent simulations to balance accuracy and efficiency. Although this grid independence test was based on global outlet parameters, the selected mesh was considered adequate for the subsequent comparative analysis of the investigated operating conditions.

Table 1. Grid independence validation results at the boiler outlet under BMCR condition.

Mesh Resolution	Number of Cells/×10⁶	Outlet Temperature/K	Outlet NO_x/ppm	Outlet Average Velocity/m·s⁻¹
Coarse	1.05	1245	283	12.70
Medium	2.42	1215	264	12.10
Fine	3.69	1212	262	12.04

2.3. Mathematical Model

2.3.1. Reaction Model

Considering the turbulent nature of high-temperature flue gas in the furnace, combustion was simulated using the species transport model, which is applicable to a wide range of gaseous combustion problems. The reaction rate was calculated using the finite-rate/eddy dissipation model, accounting for both kinetic and turbulence effects [28]. Turbulent flow was modeled using the realizable k–ε two-equation model, as follows:

$$\frac{\partial(\rho \mathrm{k})}{\partial t}+\frac{\partial}{\partial \mathrm{x}_i}\left(\rho u_i k\right)=\frac{\partial}{\partial \mathrm{x}_i}\left[\left(\mu+\frac{\mu_{\mathrm{t}}}{\sigma_k}\right)\frac{\partial k}{\partial \mathrm{x}_i}\right]+G_k-\rho\varepsilon \tag{1}$$

$$\frac{\partial}{\partial t}(\rho\varepsilon)+\frac{\partial}{\partial \mathrm{x}_i}\left(\rho\varepsilon \mathrm{u}_i\right)=\frac{\partial}{\partial \mathrm{x}_i}\left[\left(\mu+\frac{\mu_{\mathrm{t}}}{\sigma_\varepsilon}\right)\frac{\partial \varepsilon}{\partial \mathrm{x}_j}\right]+\rho C_1 S\varepsilon-\rho C_{2\varepsilon}\frac{\varepsilon^2}{k+\sqrt{v\varepsilon}} \tag{2}$$

where k represents the turbulent kinetic energy, ρ denotes the fluid density, u_i represents the velocity component in the i-th direction, G_k denotes the generation of turbulent kinetic energy due to the mean velocity gradients, μ represents the molecular viscosity, μ_t denotes the turbulent viscosity, S denotes the mean strain rate, ε represents the dissipation rate, $\sigma_k = 1.0$, $\sigma_\varepsilon = 1.2$, $C_{2\varepsilon} = 1.9$.

The particle size distribution of the fuel was characterized by the Rosin–Rammler distribution. Particle motion was simulated using a Lagrangian stochastic particle trajectory model, described in Equation (3) [29]. The devolatilization process was modeled via

a two-competing-rates model, whereas volatile combustion was described by the mixture fraction–probability density function model. Sulfur release during devolatilization was treated as proportional to the volatile yield, with the sulfur content of the volatile fraction set according to the proximate and ultimate analyses of each fuel. Char-bound sulfur was released during char oxidation in proportion to the carbon burnout rate, consistent with the global char combustion model employed. In the gas phase, the conversion of sulfur species was described by a global reaction mechanism: under oxygen-sufficient conditions, sulfur is oxidized to SO_2, whereas under oxygen-deficient reducing conditions (low O_2, high CO), SO_2 is reduced to H_2S via the reaction $SO_2 + 3CO + H_2O \rightarrow H_2S + 3CO_2$ [30]. This simplified global sulfur-conversion approach provides an engineering approximation suitable for comparative CFD analysis, but it does not resolve detailed multi-step sulfur chemistry. The predicted H_2S concentrations are spatially consistent with the regions of low O_2 and high CO identified in Section 3.1.3, which is physically consistent with the well-established reducing-atmosphere H_2S formation mechanism and serves as an internal consistency check on the sulfur predictions.

$$\frac{du_p}{dt} = F_D\left(u - u_p\right) + g\frac{\rho_p - \rho}{\rho_p} + F \tag{3}$$

where u_p represents the particle velocity, u represents the fluid velocity, ρ_p represents the pulverized coal density, ρ denotes the continuous phase fluid density, F_D denotes the drag force coefficient per unit particle mass, and F represents the resultant force excluding gravity and buoyancy.

The P1 radiation model was employed to calculate radiative heat transfer, as expressed in Equation (4), which accounts for the effects of scattering and particulate phases while maintaining relatively low computational cost [31].

$$q_r = -\frac{1}{3\left(a + \sigma_s\right) - C\sigma_s}\nabla G \tag{4}$$

Where q_r denotes the radiative heat flux, a represents the absorption coefficient, σ_s represents the scattering coefficient, C represents the linear anisotropic phase function, and G represents the incident radiation.

Char combustion was described by a kinetics/diffusion-controlled reaction rate model, shown in Equation (5), which provides a more realistic representation of the actual char combustion process.

$$\frac{dm_p}{dt} = -A_p p_{ox}\frac{D_0 R}{D_0 + R} \tag{5}$$

where p_{ox} denotes the partial pressure of the oxidizer during combustion, A_p represents the particle surface area, D_0 represents the diffusion coefficient, and R represents the kinetic rate coefficient.

Furthermore, NOx formation was evaluated in a post-processing manner to decouple the flow and main combustion calculations from the pollutant formation, thereby saving computational resources. Thermal NO_x was modeled using the extended Zeldovich mechanism, whereas fuel NO_x was described by the De Soete model, with a char nitrogen conversion factor of 0.5 [32].

2.3.2. Corrosion Degree Assessment Model

In accordance with the "Technical Guidelines for Wall Atmosphere Testing in the High-Temperature Corrosion Zone of Coal-Fired Boiler Water-Cooled Walls" compiled by China Energy Investment Corporation, the volume fractions of O_2, CO, and H_2S were

used to evaluate the severity of high-temperature corrosion [33,34]. Based on these indicators, the risk levels of high-temperature corrosion on water-cooled walls were categorized, as shown in Table 2. Although the guideline was originally developed for coal-fired boilers, it remains applicable for identifying relative corrosion-risk regions under biomass–coal cofiring conditions. Previous studies have demonstrated that local reducing atmospheres characterized by oxygen deficiency, elevated CO concentrations, and sulfur-containing gases are still the primary driving factors for water-wall corrosion in cofiring systems. It should be noted that the present CFD corrosion assessment focuses exclusively on sulfidic corrosion driven by reducing-atmosphere conditions (O_2, CO, and H_2S concentrations). Alkali metal (K, Na) and chlorine-induced corrosion mechanisms are not modeled in the present numerical framework. The interaction between alkali/chloride deposition and sulfidic corrosion under cofiring conditions represents an important avenue for future work and is discussed further in the Conclusions.

Accordingly, each wall-adjacent CFD cell was classified using a stepwise O_2–CO–H_2S criterion. The local O_2 volume fraction was first examined to identify oxygen-deficient regions. Cells with $O_2 \geq 2\%$ were assigned to the "Nothing" category. For oxygen-deficient cells, the corrosion severity was then determined from the CO and H_2S volume fractions using an "OR" logic; the higher severity indicated by either species was adopted. This procedure yielded the spatial distribution of relative corrosion severity on the water-cooled walls. Because the "OR" logic adopts the highest severity indicated by either CO or H_2S, the resulting classification should be interpreted as a conservative relative corrosion-risk map rather than a direct prediction of metal loss. Each cell on the water-cooled wall was further evaluated to obtain a detailed distribution of the corrosion severity.

Table 2. Classification of high-temperature corrosion risk levels.

Corrosion Degrees	Volume Fractions of Chemical Species		
	O_2	CO	H_2S
Nothing	$\geq 2\%$		
Slight	$1\% \leq O_2 < 2\%$	$\leq 0.1\%$	
Moderate	$< 1\%$	$1\% < CO \leq 3\%$	$0.01\% \leq H_2S \leq 0.02\%$
Severe	$< 1\%$	$> 3\%$	$\geq 0.02\%$

The corresponding code was developed using Visual Studio (2019) and compiled and loaded into the Fluent software (2024 R2) environment for numerical simulations. The results enabled the accurate extraction of both the spatial distribution of corrosion severity throughout the furnace and the proportional area of each severity level, serving as a vital database for subsequent corrosion assessment and design improvements.

2.3.3. Wear Model

The Oka erosion model was selected for numerical simulations based on extensive experimental data and by taking into account the erosion caused by fly ash particles impacting diversion plates and flue duct walls, as presented in Equations (6)–(9) [35,36]. This model adequately incorporates the physical properties of both the target metal and the particles, and it is applicable to any combination of materials, impact angles, and velocities. The physicochemical properties of the erodent particles required by the Oka model are summarized in Table 3. The simulation only accounts for fly ash particles resulting from complete combustion. Under the BMCR operating condition, the boiler exhibits high combustion efficiency with a minimal carbon content in the fly ash. Consequently, the mass concentration of unburned particles is extremely low, rendering their contribution to erosion negligible.

$$E(\alpha)=g(\alpha)E_{90} \tag{6}$$

$$g(\alpha)=(\sin\alpha)^{n_1}\left(1+H_v(1-\sin\alpha)\right)^{n_2} \tag{7}$$

$$E_{90}=10^{-9}K_1(H_v)^{k_2}\left(\frac{V_p}{V_{ref}}\right)^{k_3}\left(\frac{d_p}{d_{ref}}\right)^{k_4} \tag{8}$$

$$e_r=\rho_w E(\alpha) \tag{9}$$

where H_v represents the material's Vickers hardness; n_1 and n_2 denote the specified coefficients; v_p represents the particle–wall relative velocity; d_p represents the particle diameter; V_{ref} represents the reference velocity; d_{ref} represents the reference particle diameter; ρ_w represents the fly ash particle density; k_1, k_2, k_3, and k_4 represent reference coefficients, and e_r represents the erosion rate.

Table 3. Parameters and assumptions used in the Oka erosion model.

Parameter	Coal Ash	Biomass Ash(CS/WS/RS)
Density (kg·m^{-3})	2200	1900/1850/2100
Particle Vickers hardness (HV)	1000	550/480/750
Shape factor (ψ)	0.90	0.72/0.75/0.68
Post-combustion mean diameter (μm)	120	120/120/120
Rosin-Rammler distribution index (n)	1.2	1.1/1.1/1.1

2.4. Simulation Conditions

Simulations were conducted based on the boiler maximum continuous rating (BMCR) condition. The fuels used comprised anthracite (AN) and three types of crop residues: wheat straw (WS), rice straw (RS), and corn stover (CS). A total of seven operating conditions were established, as summarized in Table 4, including pure coal combustion and cofiring cases with a 30% biomass blending ratio (by mass). The proximate and ultimate analyses of the fuels are presented in Table 5. Furthermore, to provide a mechanistic foundation for discussing ash deposition, mineral evolution, and high-temperature corrosion, the comprehensive chemical compositions of the fuel ashes were determined via X-ray fluorescence (XRF) spectroscopy and are explicitly incorporated. The experimental baselines of these key ash-forming oxides (such as SiO_2, Al_2O_3, and K_2O) yield crucial empirical constraints for interpreting the localized formation of low-melting-point eutectics and the resultant corrosion/erosion risks evaluated in the subsequent sections.

Table 4. Research conditions used in this study.

Operating Mode	Proportion of Pulverized Coal/%	Proportion of Corn Stover/%	Proportion of Wheat Straw/%	Proportion of Rice Straw/%	Biomass Injection Location	Coal Injection Location
AN	100	0	0	0	-	ABCDEF
AN7CS3-A	70	30	0	0	A	BCDEF
AN7WS3-A	70	0	30	0	A	BCDEF
AN7RS3-A	70	0	0	30	A	BCDEF
AN7CS3-AB	70	30	0	0	AB	CDEF
AN7WS3-AB	70	0	30	0	AB	CDEF
AN7RS3-AB	70	0	0	30	AB	CDEF

Table 5. Ultimate analysis, proximate analysis, and ash compositions of fuels.

Samples	Proximate Analysis/wt%				Ultimate Analysis/wt%					Ash Composition/wt%			LHV/MJ·kg^{-1}
	M_{ad}	A_{ad}	V_{ad}	FC_{ad}	N	C	H	S	O	SiO_2	K_2O	Al_2O_3	
AN	0.43	39.17	21.31	39.09	0.74	46.39	3.36	0.23	10.49	50.5	0.45	45.55	30.135
RS	5.29	15.78	62.98	15.95	0.53	37.86	4.64	0.07	41.70	80.0	8.5	2.0	15.527
CS	5.09	12.96	64.59	17.36	0.61	40.01	5.29	0.15	40.50	72.5	11.5	1.5	17.432
WS	4.73	16.86	62.50	15.91	0.40	38.41	4.56	0.11	41.18	73.0	9.5	1.5	13.375

The inlet temperature and mass flow rate for coal and biomass particles were specified according to boiler design parameters. The particle size distribution followed the Rosin–Rammler function [37], with maximum, minimum, and mean diameters set to 220, 70, and 120 μm, respectively, for pulverized coal and to 300, 50, and 120 μm, respectively, for biomass. The particle inlet temperature was consistent with the primary air stream temperature, and the inlet velocity of both fuel types was set equal to the primary air velocity. Boundary conditions in Fluent were defined as follows: the primary air, secondary air, and over-fire air inlets were set as the velocity inlets; the outlet was defined as the pressure outlet at −80 Pa; and furnace walls were treated with the standard wall function and a no-slip condition. To validate the applicability of the standard wall function, the near-wall y^+ values were examined across all wall-adjacent cells. Post-processing of the converged flow field showed that the area-weighted average y^+ value in the main combustion zone (burner region) was approximately 55, and in the burnout zone approximately 50, with the vast majority of near-wall cells falling within the range of 30–100. These values are well within the valid logarithmic-layer range ($30 \leq y^+ \leq 300$) recommended for standard wall functions, confirming that the mesh resolution near the walls is appropriate and that the wall-function-based turbulence treatment is consistent with the near-wall flow regime at the locations of maximum erosion. Thermally, the wall temperature of the burner zone was set to 800 K, those of the reburning and burnout zones were set to 690 K, and that of the cold hopper bottom was set to 470 K, with a wall emissivity of 0.8. The air distribution parameters are listed in Table 6.

Table 6. Air distribution parameters of the boiler.

Project	Wind Speed/m·s^{-1}	Wind Ratio/%	Air Temperature/K
Primary air	25	20	571
Secondary air	52	64	637
Over-fire air	47	16	637

The simulation employed the Semi-Implicit Method for Pressure-Linked Equations (SIMPLE) algorithm for three-dimensional steady-state coupling of flow and combustion. Spatial discretization of the convective terms was handled using a second-order upwind scheme to ensure numerical accuracy. Convergence was considered achieved when the residuals for the energy equation fell below 10^{-6} and below 10^{-4} for all other variables.

2.5. Model Validation

The simulated and design specification data are presented in Table 7, where the reference values are the guaranteed design specification parameters provided by the boiler manufacturer for the specific 660 MW unit studied in this work under 100% BMCR conditions. The discrepancy in the flue gas temperature at the furnace outlet is within 8%, whereas the measured NO_x concentration closely aligns with the simulation results, showing a deviation of less than 2%. Therefore, the models selected for the numerical simulations were considered reasonable and reliable and were applied to simulate various

operating conditions. While detailed in situ experimental data within the full-scale furnace is practically unattainable, the reliability of the established model can be further supported by the qualitative assessment of the internal reacting fields. As will be discussed in Section 3.1.2, the predicted internal species profiles, such as the rapid depletion of O_2 and the generation/oxidation of CO along the furnace height, strictly follow the fundamental mechanisms of staged combustion. Furthermore, the agreement in outlet NO_x provides partial support for the combustion model, although additional spatial validation would strengthen confidence in the predicted wall-atmosphere fields. Nevertheless, combined with the trend-wise consistency of internal profiles, the integrated CFD framework is considered acceptable for the subsequent investigations. However, the absence of direct measurements of near-wall H_2S concentration, corrosion rate, and erosion rate remains a limitation of the present validation and should be considered when interpreting the absolute risk levels.

Additional confidence in the model is established through comparison with previously published CFD studies on large-scale pulverized coal and biomass co-firing furnaces. The predicted furnace outlet temperature (1221 K) and the overall temperature distribution pattern are consistent with results reported for similar 600 MW utility boilers under comparable operating conditions [38]. The staged-combustion O_2 depletion profile—showing near-complete O_2 consumption in the primary combustion zone and residual concentrations below 3% at the furnace exit—agrees qualitatively with measured axial O_2 profiles documented in the literature for staged low-NO_x burner configurations [39]. Similarly, the simulated CO generation peak in the sub-stoichiometric primary zone, followed by near-complete burnout upstream of the furnace exit, is physically consistent with well-established combustion theory and has been corroborated in comparable numerical studies [40]. It should be noted that direct in situ measurement of species distributions, wall temperatures, or corrosion-related quantities within an operating full-scale utility boiler is practically infeasible due to extreme thermal and operational constraints. The two available plant measurements (furnace outlet temperature and NO_x emissions) represent the key global quantities accessible under industrial operating conditions and are widely adopted as primary validation targets in the peer-reviewed CFD literature on utility-scale boilers. Taken together, the quantitative agreement with plant data, the physical consistency of the internal field predictions with fundamental combustion theory, and the alignment of key trends with published benchmark results collectively substantiate the reliability of the proposed CFD framework for predicting corrosion distribution, erosion behavior, and wall-level spatial patterns under the investigated operating conditions.

Table 7. Comparison of the simulated and design specification values of some critical parameters.

Parameters	Simulated Value	Design Specification Value	Relative Error/%
Furnace outlet flue temperature/K	1221	1135	7.6
Furnace outlet NO_x concentration/ppm	304	298	2.0

3. Results and Discussion

3.1. Analysis of Biomass Cofiring Characteristics Under Multiple Operating Conditions

3.1.1. Ash Mineral Analysis

Detailed analyses of the ash mineralogy were conducted in our previous study [41] using the same coal and biomass samples (corn stover, rice straw, and wheat straw) employed in the present work, thereby directly providing the mineralogical database to support the interpretation of corrosion and erosion behaviors for the AN, AN7CS3, AN7RS3, and AN7WS3 fuel blends. During the co-combustion of biomass and coal, potassium and

sodium from the biomass interact with alumina and quartz in the coal, forming low-melting-point minerals, such as potassium feldspar and albite. Specifically, the ash of the AN7CS3 sample primarily comprises potassium feldspar, anorthite, and quartz; the AN7WS3 ash comprises albite, anorthite, and quartz; and the AN7RS3 ash contains predominantly potassium feldspar, albite, and anhydrite.

Notably, as highlighted in previous studies [42], the interaction between soluble potassium from biomass and silica can lead to the formation of K_2O/SiO_2 eutectics. These eutectics possess extremely low melting points, promoting their tendency to "plate out" on superheater surfaces rather than water-cooled walls, significantly increasing the risk of silicate melt-induced slagging. Furthermore, for fuels like unwashed rice straw, the amorphous silica in the plant cell walls can transform into a much denser cristobalite form in high-temperature zones. This cristobalite has a high Mohs hardness, which exacerbates the erosion of boiler heating surfaces when entrained in the flue gas. On the one hand, hard mineral particles such as quartz and anhydrite entrained in the flue gas cause erosion on boiler heating surfaces. On the other hand, low-melting-point minerals such as albite and potassium feldspar form molten slag at relatively low temperatures, further promoting high-temperature corrosion and erosion of heating surfaces. Moreover, the coupling effects among ash minerals after biomass blending considerably influence the temperature distribution within the furnace and alter the composition of the flue gas. It should be noted, however, that the present CFD model does not dynamically couple ash deposition or slagging effects on wall heat transfer, temperature fields, or flue gas species distributions. The ash mineralogy analysis presented here therefore serves as a qualitative contextual framework for interpreting the corrosion and erosion predictions, rather than as a coupled input to the numerical model. The potential influence of this simplification on the predicted results is discussed in the Conclusions.

3.1.2. Temperature Field Analysis

The temperature distribution characteristics serve as a key indicator for evaluating the combustion efficiency, heat transfer performance, and operational reliability of coal-fired boilers [43]. Figure 2 shows the temperature contours of the central furnace cross section under various operating conditions. Biomass cofiring does not significantly alter the symmetry of the original temperature field. In all cases, the high-temperature zone remains concentrated around the main burners. The temperatures in both the central zone and the cold hopper region slightly decrease after biomass blending compared with those in the pure coal combustion case. The main reasons are as follows: (1) Biomass fuel is highly flammable and has a lower calorific value. This causes rapid ignition and burnout in the furnace, reducing heat accumulation in the central zone. (2) The high volatile content of biomass results in rapid release and combustion of most volatiles shortly after injection, leaving less fuel to reach the cold hopper region. This reduces the heat load in the lower part of the furnace center, moderately decreasing the temperature.

Figure 3 presents the cross-sectional average temperature distribution along the furnace height under various operating conditions. With biomass cofiring, the overall temperature profiles along the furnace height remain generally similar across all cases. In the main combustion zone, rapid fuel combustion releases a large amount of heat, resulting in high furnace temperatures that peak at approximately 20–22 m before the injection of over-fire air. At approximately 25.5 m, the introduction of over-fire air noticeably decreases the temperature in this region because of air dilution and local cooling. Meanwhile, the over-fire air promotes the combustion of unburned fuel, leading to a slight temperature recovery downstream. As the amount of combustible fuel decreases toward the upper furnace, the combustion process approaches completion, and the temperature gradually declines.

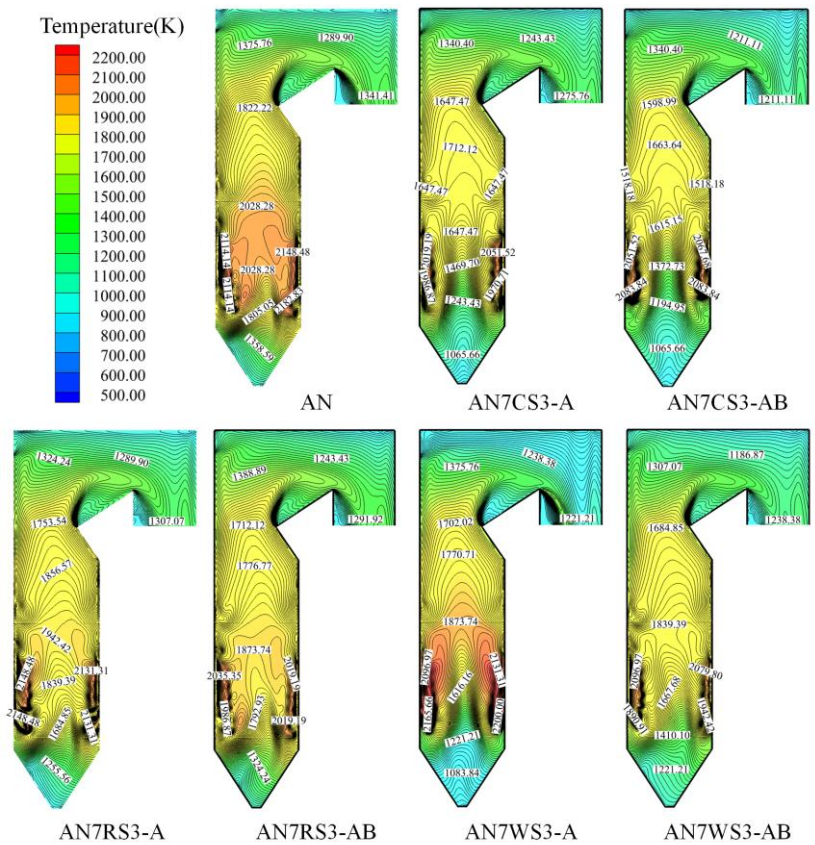

Figure 2. Temperature distribution of the central furnace cross-section.

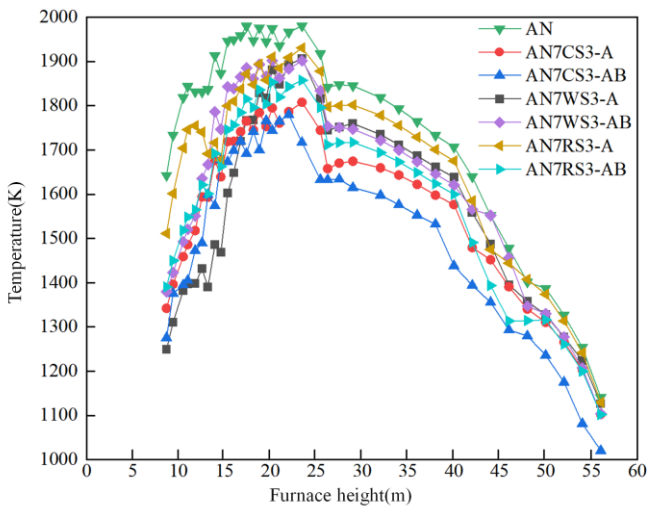

Figure 3. Average temperature distribution across furnace height for different operating conditions.

Compared with pure coal combustion (AN), biomass cofiring reduces the peak furnace temperature under all cofiring conditions. This reduction can be attributed to the lower calorific value and different combustion characteristics of biomass compared with coal, which reduce the local heat release intensity and consequently lower the peak temperature. When the biomass injection position is located at the lower layer A, the temperature at lower furnace elevations, approximately 8–15 m, is relatively higher because biomass particles have a lower ignition temperature and higher volatile content, leading to earlier ignition and more intense local combustion. By contrast, elevating the injection po-

sition to layer AB shifts volatile release and combustion reactions to higher furnace elevations, resulting in a more spatially distributed heat-release profile and lower temperatures in the lower furnace region.

Figure 4 shows the temperature distribution contours at the primary-air nozzle cross section under different operating conditions. The cofiring of biomass expands the low-temperature region in the furnace center owing to the lower ignition temperature and heating value of biomass compared with those of pulverized coal, which promotes rapid ignition and complete combustion once injected into the furnace. The accelerated heat release forms a more heterogeneous temperature field, thereby enlarging the low-temperature zones in the furnace core.

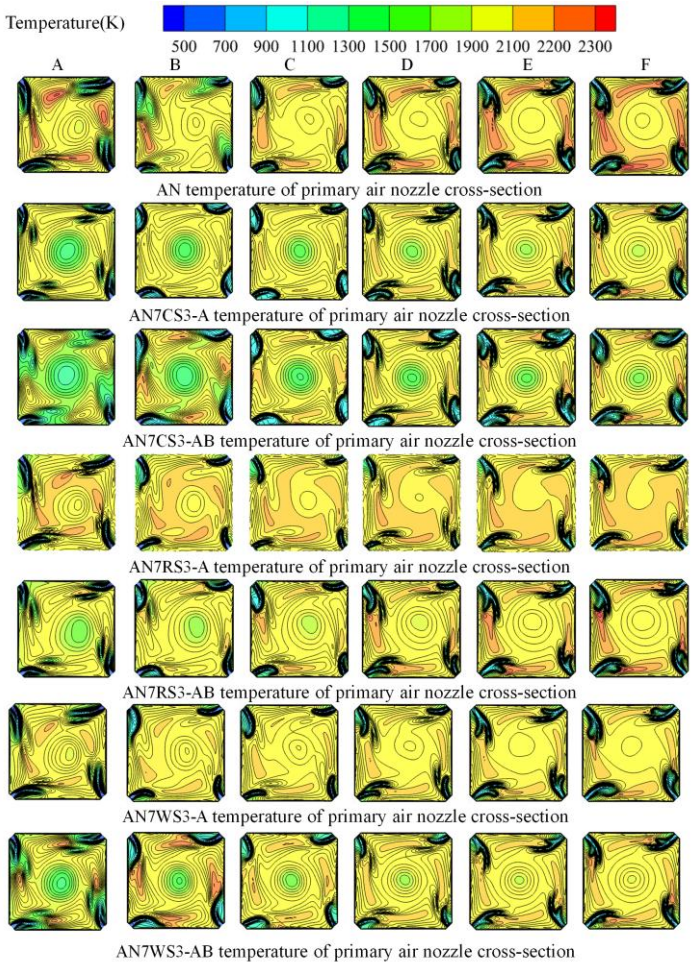

Figure 4. Temperature distribution contour at the primary-air nozzle cross section. (A)-(F) denote the six primary air nozzles.

The low-temperature region at the center of the biomass nozzle cross section gradually diminishes when the elevation of the biomass injection port increases. This spatial transition is fundamentally driven by the high volatile content of the biomass (approx. 63 wt.%, as shown in Table 5). When injected at lower levels (layer A), the rapid release and intensive combustion of these volatiles lead to severe localized oxygen depletion and a subsequent thermal deficit. By elevating the injection port to layer AB, the intensive volatile reactions are spatially distributed along the furnace height, as confirmed by the temperature contours in Figure 4.

3.1.3. Flue Gas Composition Analysis

Flue gas composition serves as a critical indicator for the evaluation of pollutant emissions and their environmental impacts. Moreover, it provides an important basis for analyzing high-temperature corrosion risks in boilers [44]. Figure 5 shows the distribution of O_2, CO, and CO_2 volume fractions in the furnace.

Figure 5a shows the O_2 volume fraction contours at the central furnace cross section under different operating conditions. The spatial distribution of the O_2 volume fraction exhibits a consistent pattern across all cases. The O_2 concentration reaches its minimum in the vicinity of the burner outlets, primarily because the fuel carried by the primary air undergoes rapid ignition and combustion upon entering the furnace, consuming large amounts of oxygen and reducing the O_2 content near the primary-air nozzles to nearly zero. Unburned fuel continues to react in the region above the over-fire air nozzles, further depleting oxygen and resulting in similarly low O_2 concentrations in this zone. Cofiring biomass noticeably decreases the O_2 volume fraction at the furnace center, which can be attributed to the higher volatile content of biomass. The abundant volatiles demand additional oxygen to sustain their oxidation during the initial combustion stage, increasing O_2 consumption and lowering the measured O_2 concentration.

Figure 5b presents the distribution of average O_2 volume fraction along the furnace height under different operating conditions. Variations in O_2 volume fraction are consistent across all cases. In the main combustion zone, the combustion of fuel consumes a substantial amount of O_2, remarkably reducing the O_2 volume fraction. With the injection of the over-fire air, the O_2 concentration begins to recover. However, unburned fuel continues to consume O_2 in the burnout zone, causing the O_2 volume fraction to decrease again until the complete combustion of the fuel and the stabilization of the O_2 concentration. Compared with pure coal combustion, biomass cofiring generally reduces the O_2 volume fraction owing to the higher volatile content of biomass, which rapidly consumes O_2 during combustion, thereby reducing the O_2 volume fraction in the cold ash hopper and the main combustion zone. Furthermore, because more fuel remains unburned in the main combustion zone during cofiring, a larger quantity of fuel continues to burn in the burnout zone, resulting in a lower O_2 concentration in this region.

Figure 5c presents the CO volume fraction contours at the central furnace cross section for both pure coal combustion and cofiring with biomass. The CO volume fraction variations are largely similar across all conditions, with the highest concentrations observed near the primary air injection points in the main combustion zone. This is attributed to the rapid combustion of the fuel entering the furnace, which consumes a significant amount of oxygen, leading to insufficient oxygen supply in the primary combustion area and thereby promoting incomplete combustion and resulting in substantial CO production. Specifically, the CO volume fraction reaches its peak near the primary air nozzles, while other regions exhibit much lower CO concentrations, with most areas having values close to zero. Compared with pure coal combustion, the addition of biomass exacerbates the oxygen depletion owing to the rapid consumption of oxygen during biomass combustion in the furnace. The partial oxidation of biomass generates additional CO, increasing CO volume fractions near the burner nozzles.

Figure 5d shows the average CO volume fraction distribution across the horizontal cross section of the boiler for both pure coal combustion and cofiring with biomass. Under pure coal combustion conditions, the pulverized coal in the main combustion zone consumes a significant amount of O_2. The primary air supply is insufficient to fully combust the coal particles, resulting in the formation of a large amount of incomplete combustion products and, consequently, a high CO volume fraction in this area. The injection of secondary air increases the O_2 concentration, allowing for more complete combustion of the coal particles, which leads to a decrease in the CO volume fraction. Upon cofiring biomass, the higher volatile content of the biomass facilitates its ignition and complete combustion.

This increases the O_2 consumption in the primary combustion zone, exacerbating the incomplete combustion of coal particles and causing a marked rise in the CO volume fraction, which peaks near the biomass injection point. The influence of different nozzle positions on the final CO volume fraction is minimal, as the fuel is almost completely combusted in all conditions, and the CO volume fraction near the furnace outlet approaches zero.

Figure 5e presents the CO_2 volume fraction contours at the central furnace cross section for both pure coal combustion and cofiring with biomass. The distribution patterns of CO_2 volume fraction within the furnace are similar across all conditions. The highest CO_2 volume fraction is observed near the burner nozzles, and the CO_2 concentration at the furnace center gradually rises as the furnace height increases. Compared with pure coal combustion, the CO_2 volume fraction at the furnace outlet increases when biomass is injected from layer A. However, when biomass is injected from layer AB, the CO_2 volume fraction at the furnace outlet decreases.

Figure 5f shows the average CO_2 volume fraction distribution across the horizontal cross section of the boiler for both pure coal combustion and cofiring with biomass. CO_2 volume fraction variations are generally consistent across all conditions. The CO_2 volume fraction is higher in the cold ash hopper region, while it exhibits significant fluctuations (first increasing and then decreasing) throughout the combustion process in the main combustion zone. The injection of burnout air decreases the CO_2 volume fraction, followed by its increase as some incompletely combusted fuel undergoes further oxidation and gradual stabilization. Compared with pure coal combustion, the cofiring scenario when biomass is injected from layer A generates a higher CO_2 volume fraction, indicating that biomass injection at the lowest layer promotes combustion reactions, thereby increasing CO_2 production. Conversely, when biomass is injected from layer AB, the CO_2 volume fraction in the cofiring scenario is lower, indicating that this injection method helps reduce carbon emissions.

The simulated spatial distributions of these flue gas species play a critical role in establishing the localized boundary conditions that govern the downstream high-temperature corrosion and erosion behaviors on the furnace walls. Specifically, the presence of high CO concentrations paired with severe local O_2 deficiencies near the lower injection layers creates a strongly reducing atmosphere, which typically accelerates the destruction of protective oxides on the water-wall tubes and favors the formation of corrosive iron sulfides. Conversely, the increased residual O_2 fields and lowered CO presence under layer AB cofiring conditions help mitigate this aggressive chemical environment. A more comprehensive, quantitative correlation between these gas-phase multi-species matrices and the solid-phase wall degradation processes will be systematically evaluated in Section 3.2.

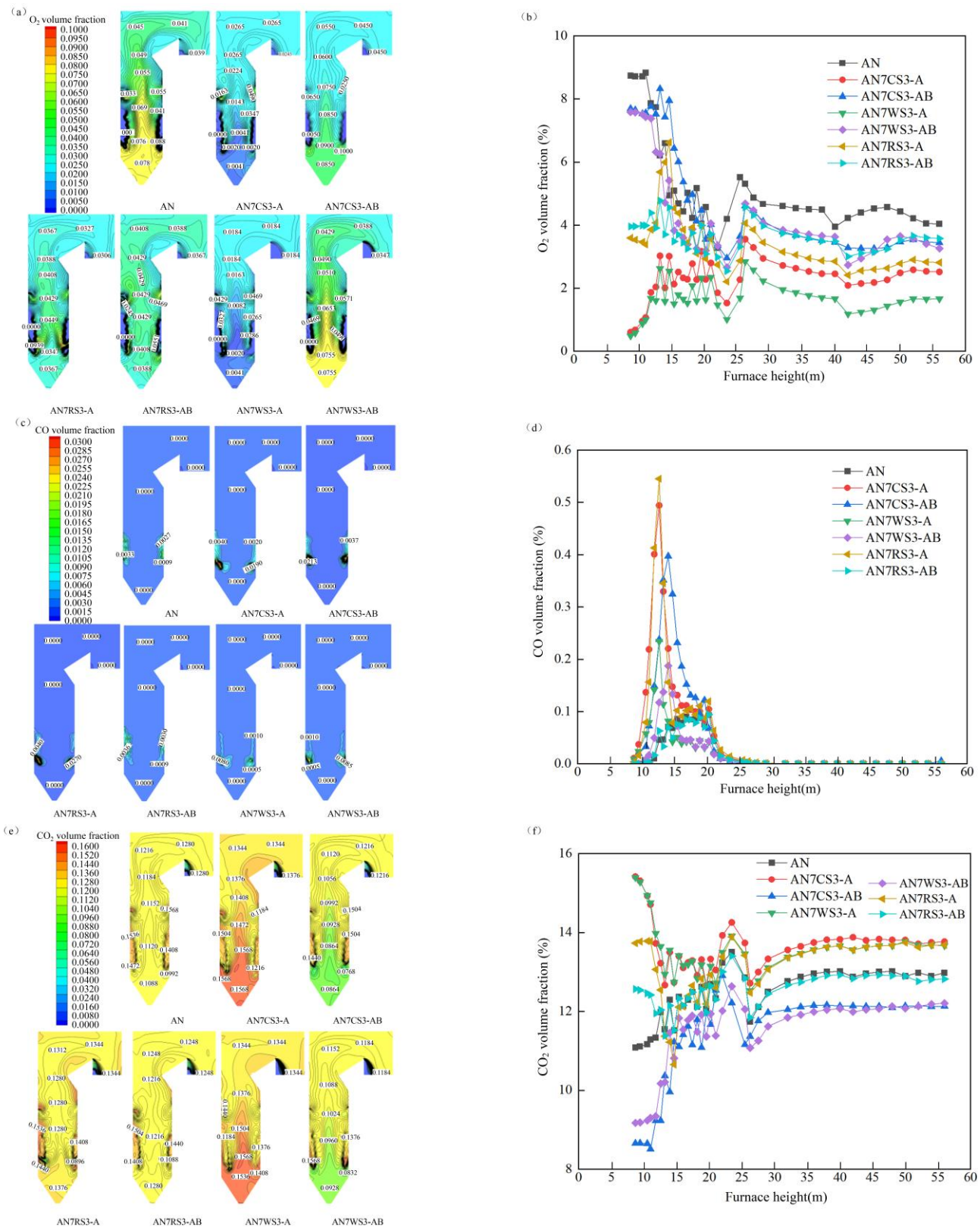

Figure 5. Distribution of O_2, CO, and CO_2 volume fractions in the furnace: (**a**) contour map of O_2 volume fraction distribution at the central furnace cross section, (**b**) distribution of the average O_2 volume fraction along the furnace height, (**c**) contour map of CO volume fraction distribution at the central furnace cross section, (**d**) distribution of the average CO volume fraction along the furnace height, (**e**) contour map of CO_2 volume fraction distribution at the central furnace cross section, and (**f**) distribution of the average CO_2 volume fraction along the furnace height.

3.2. Evaluation of Corrosion Degree of Boiler Heat Exchange Surfaces

3.2.1. Analysis of Corrosive Gases

The distribution contours of O_2, CO, and H_2S volume fractions on the furnace wall for different operating conditions are shown in Figure 6. As shown in Figure 6a, the O_2 concentration is higher in the cold ash hopper region, while the O_2 volume fraction is relatively low in the main combustion zone owing to the substantial O_2 consumption as the fuel combusts upon injection through the primary air nozzles. In contrast, the oxygen concentration is lower above the burnout air nozzle as the unburned fuel from the main combustion zone continues to burn in this area, consuming additional O_2 and lowering the O_2 volume fraction.

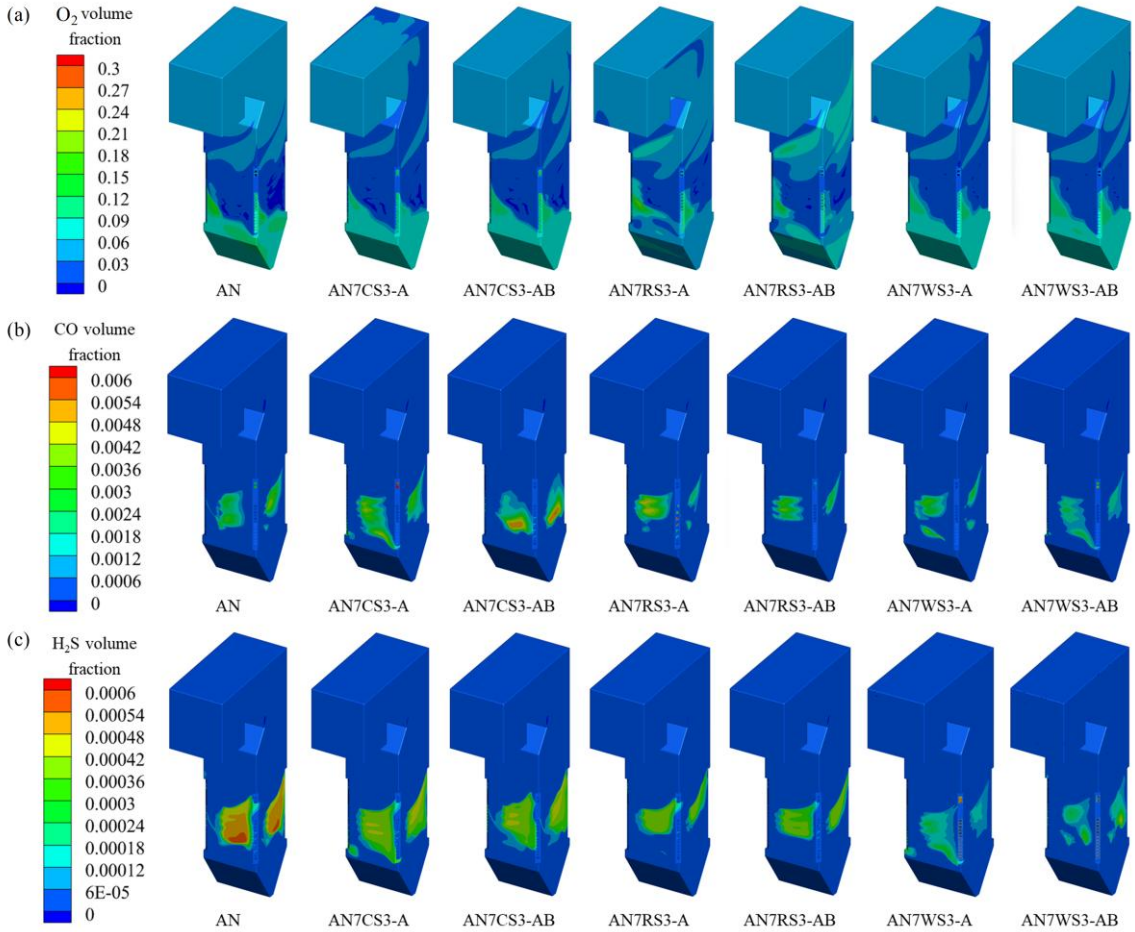

Figure 6. Distribution contours of (**a**) O_2, (**b**) CO, and (**c**) H_2S volume fractions on the furnace wall.

As shown in Figure 6b, the CO volume fraction distribution pattern on the furnace wall is consistent across all conditions, with the highest concentrations occurring near the main combustion zone because of the fuel entering the furnace with the primary air, considerably consuming oxygen and resulting in insufficient oxygen in the main combustion zone. This causes incomplete fuel combustion, leading to substantial CO generation. The CO is primarily concentrated in the main combustion zone, while the CO volume fraction in other regions is nearly zero.

In pulverized coal boilers, when the local air supply is insufficient during combustion, the sulfur in the coal or SO_2 generated during combustion can be converted into H_2S, which is a key factor contributing to high-temperature corrosion. H_2S is primarily concentrated in the main combustion zone, as shown in Figure 6c [45]. This is due to the lower

oxygen concentration in this region, where the pulverized coal fails to fully combust, generating a significant amount of CO and creating a strongly reducing atmosphere, which increases H_2S concentrations. The H_2S volume fraction on the furnace wall consistently exceeds the corrosion-risk threshold of 0.01% across all operating conditions, indicating that sulfidic corrosion may occur on the boiler wall surfaces under all operating conditions.

3.2.2. Evaluation of Heat Surface Corrosion Degree Under Multiple Operating Conditions

The corrosion degree distributions of the furnace wall simulated under different operating conditions are shown in Figure 7. The corrosion in the boiler primarily occurs in the main combustion zone, with minimal corrosion observed in the cold ash hopper and the top of the furnace. Severe corrosion is not present on the boiler wall; moderate corrosion is rare, and light corrosion predominantly occurs near the water-cooled wall.

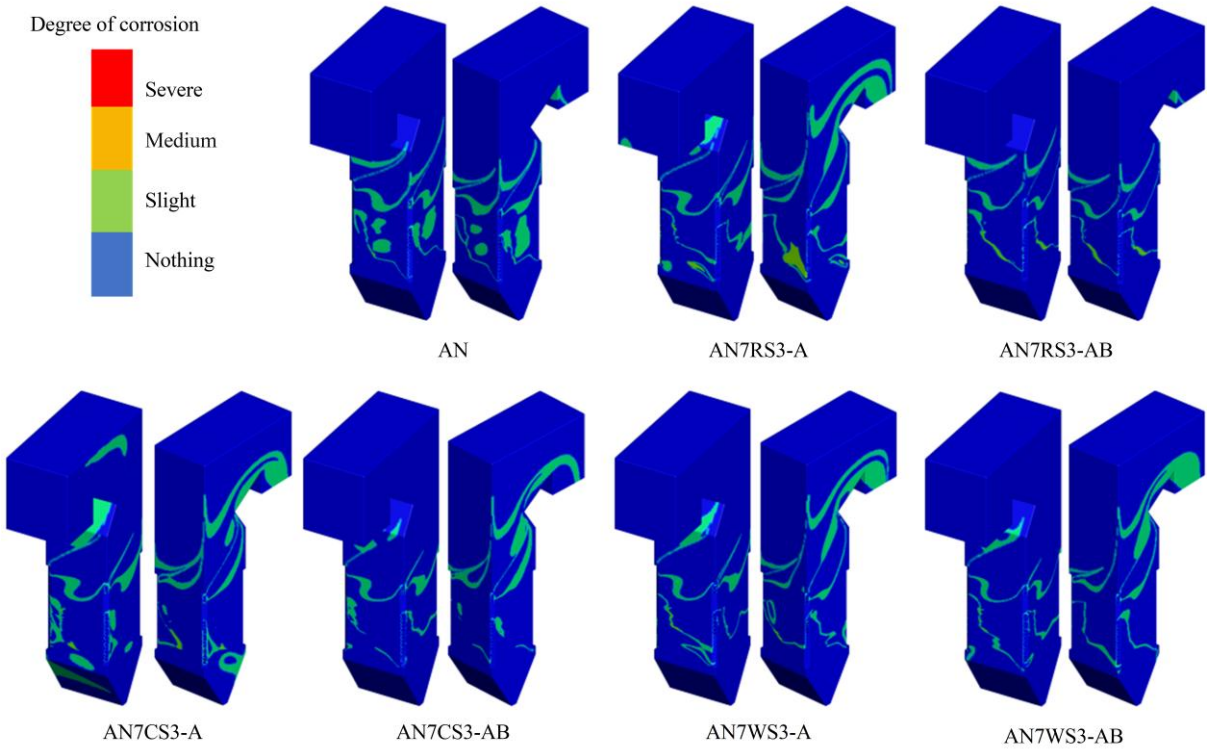

Figure 7. Distribution contours of furnace wall corrosion degree under different operating conditions.

Table 8 presents the proportions of areas with different corrosion degrees under various operating conditions. Compared with pure coal combustion, the injection of biomass from layer A increases the corrosion degree of the boiler wall. In particular, when 30% CS is injected from layer A, the proportion of light corrosion in the boiler increases by 70.91%; when 30% RS is injected from layer A, the proportion of moderate corrosion increases by a factor of 11. In contrast, injecting biomass from layer AB reduces the overall corrosion degree of the boiler. For example, when 30% RS is injected from layer AB, the proportion of light corrosion decreases by 34.4%, while the proportion of moderate corrosion decreases by 40%.

Table 8. Proportion of areas with different corrosion degrees under various operating conditions.

Operating Mode	Nothing/%	Slight/%	Moderate/%	Severe/%
AN	92.73	7.22	0.05	0
AN7CS3-A	87.44	12.34	0.22	0

AN7RS3-A	90.48	8.92	0.60	0
AN7WS3-A	88.96	10.87	0.17	0
AN7CS3-AB	94.12	5.44	0.44	0
AN7RS3-AB	95.23	4.74	0.03	0
AN7WS3-AB	93.74	6.18	0.08	0

3.3. Evaluation of Heat-Induced Surface Wear on the Boiler Based on the Oka Erosion Model

3.3.1. Velocity Field Analysis

The velocity field distributions within the furnace simulated under the original operating conditions (velocity contours at the central furnace cross-section and the primary air nozzle cross-section) are shown in Figure 8.

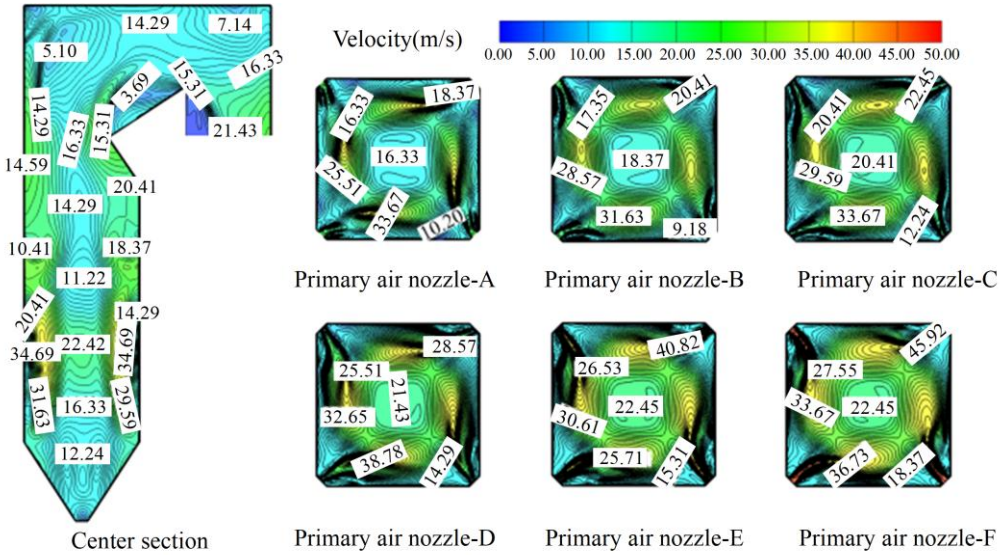

Figure 8. Velocity distribution contours at the boiler center cross-section and primary air nozzle cross-section.

The flue gas velocity field at the boiler center cross-section exhibits a symmetrical distribution, with no direct impact on the water-cooled wall. The airflow velocity near the burner nozzles is relatively high, facilitating the thorough mixing of the fuels and air and promoting rapid ignition. The airflow velocity in the cold ash hopper area decreases, and the airflow density gradually increases with the furnace height. The airflow velocity decreases after reaching the primary air nozzle F. The velocity distribution contour map at the primary air nozzle interface reveals that the circular cutting effect in the burner area is effective, with minimal interference between burners, which helps to promote fuel ignition and stable combustion. Overall, the flow field within the furnace is stable, with a reasonable velocity distribution that aligns well with actual operating conditions.

To further examine flow field variations within the furnace during the co-combustion of biomass and coal, velocity contours at the primary air nozzle cross-section were obtained for comparison, as shown in Figure 9. Circular velocity profiles are generated in all cases after biomass injection into the furnace, indicating the presence of a uniform aerodynamic field within the combustion chamber, facilitating the thorough mixing and combustion of biomass and coal. The primary air velocity variations across the different cofiring conditions are minimal, and the shapes and sizes of the circular velocity profiles are nearly identical, ensuring the stability and uniformity of the airflow.

Figure 9. Velocity distribution contours at the primary air nozzle cross-section for various operating conditions. (A)-(F) denote the six primary air nozzles.

Figure 10 shows the velocity distributions at the boiler center cross-section under different operating conditions. The flow field distribution trends are similar across all conditions, with higher airflow velocities in the furnace wall region and relatively lower velocities in the central area of the furnace. This velocity distribution characteristic aligns with the actual flow dynamics in the boiler. The higher airflow velocity near the furnace wall helps enhance heat transfer and airflow uniformity during the combustion process, while the lower velocity in the central region helps reduce the risk of local overheating, ensuring stable boiler operation. After cofiring with biomass, the airflow velocity near the burner nozzles increases, while the velocity in the furnace center decreases. This is primarily due to the higher volatile content and combustibility of biomass compared to pulverized coal. Once the biomass enters the furnace, it rapidly volatilizes and combusts, raising the temperature near the nozzle and causing gas expansion, which accelerates the airflow. In the furnace center, the lower heat content of biomass compared with that of coal reduces heat

release during combustion, lowering the temperature in this region and consequently reducing the airflow velocity.

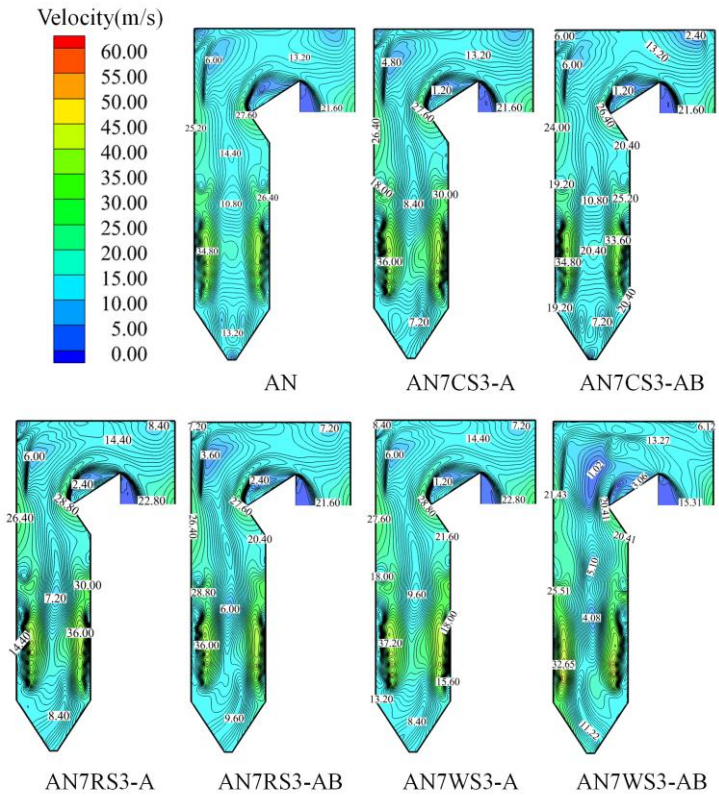

Figure 10. Velocity distribution contours at the boiler center cross section.

3.3.2. Evaluation of Heat Surface Wear Degree Under Multiple Operating Conditions

The wear conditions of the boiler were simulated under pure coal combustion based on the Oka erosion model and associated parameter settings. The wear distribution in the furnace under BMCR conditions is shown in Figure 11.

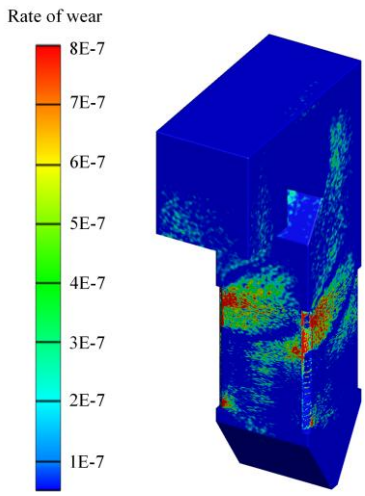

Figure 11. Distribution contour of boiler wall wear rate under pure coal combustion conditions. Note: The color scale upper limit (8×10^{-7} kg·(m^2·s)$^{-1}$) is intentionally set below the peak wear rate to highlight the spatial distribution pattern across the majority of the wall surface; the true maximum wear rate is reported in Table 9.

Under pure coal combustion conditions, the release of heat and the effects of airflow during combustion increase the airflow velocity at the burner inlet. This intensifies the impact force of coal particles, leading to significant wear in the four corner regions of the furnace. As the coal particles are blown toward the upper furnace and enter the burnout zone, the injection of burnout air destabilizes the internal flow field. Simultaneously, the higher airflow velocity increases the speed of unburned particles, making this region the most severely worn part of the furnace, with a maximum wear rate of 9.11×10^{-6}. As the coal particles continue to move upward toward the top of the furnace, the particle concentration and the overall wear degree within the furnace decrease. However, except for a few areas of noticeable wear, other regions of the furnace are also affected by particle collisions, resulting in varying degrees of wear, with the wear conditions being relatively minor.

The wear rates of different regions on the boiler wall simulated under various operating conditions are shown in Figure 12. The most significant wear on the furnace wall occurs near the burnout air nozzle because air entrance through the burnout air inlet disrupts the established airflow patterns within the furnace, destabilizing the flow field and thereby exacerbating the wear.

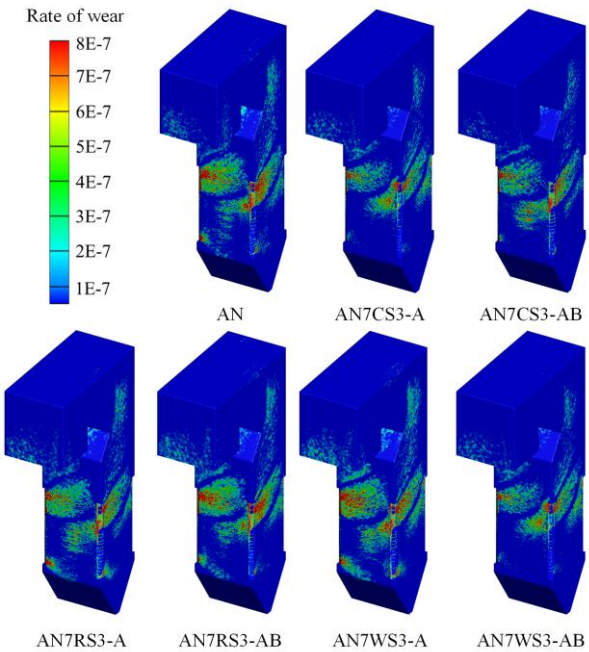

Figure 12. Distribution contours of boiler wall wear rate under various operating conditions. Note: The color scale upper limit (8×10^{-7} kg·(m^2·s)$^{-1}$) is intentionally set below the peak wear rate to highlight the spatial distribution pattern across the majority of the wall surface; the true maximum wear rate is reported in Table 9.

Table 9 presents the maximum wear rate, the average wear rate, and the sum of wear rates on the boiler wall under different operating conditions. The addition of biomass reduces both the average wear rate and the total wear rate of the furnace wall while increasing the maximum wear rate. This is because the inclusion of biomass increases the local temperatures and airflow intensities within the furnace, boosting the maximum wear rate on the boiler wall. However, the hardness of ash particles in biomass is generally lower than that of coal ash, reducing the overall impact force and, consequently, the average wear rate. Comparing the wear rates across different conditions, this study found that the addition of CS has the greatest effect on the maximum wear rate, with the injection of 30% CS from layer AB increasing the maximum wear rate by 25.1%. Moreover, the addition of

RS has the greatest impact on the average wear rate and the total wear rate, with the injection of 30% RS from layer AB reducing the average wear rate by 30.2% and the total wear rate by 57.14%.

Table 9. Boiler wall wear rate under various operating conditions.

Operating Mode	Maximum Wear Rate/kg·(m²·s)⁻¹	Average Wear Rate/kg·(m²·s)⁻¹	Sum of Wear Rate/kg·(m²·s)⁻¹
AN	9.11×10^{-6}	9.34×10^{-8}	0.021
AN7CS3-A	1.03×10^{-5}	3.88×10^{-8}	0.019
AN7RS3-A	9.76×10^{-6}	6.52×10^{-8}	0.015
AN7WS3-A	1.14×10^{-5}	9.57×10^{-8}	0.021
AN7CS3-AB	1.75×10^{-5}	8.60×10^{-8}	0.020
AN7RS3-AB	9.34×10^{-6}	3.87×10^{-8}	0.009
AN7WS3-AB	9.04×10^{-6}	7.43×10^{-8}	0.016

4. Comprehensive Safety Evaluation of Boiler Heat Exchange Surfaces

4.1. Selection of Evaluation Indicators

Six sets of data were selected as the evaluation indicators for safe boiler operation: the proportion of areas with no corrosion, the proportion of areas with slight corrosion, the proportion of areas with moderate corrosion, the maximum wear rate, the average wear rate, and the total wear rate (Table 10). Among them, the proportion of areas with no corrosion is a positive indicator, where a higher value indicates a more favorable condition for safe and stable boiler operation. Conversely, the proportion of areas with slight corrosion, the proportion of areas with moderate corrosion, the maximum wear rate, the average wear rate, and the total wear rate are negative indicators, where a higher value indicates a greater risk to safe and stable boiler operation. Normalization was performed to eliminate the dimensional influence between different indicators and ensure the comparability of the data [46]. After normalization and weighted aggregation, the comprehensive safety evaluation score represents the relative combined corrosion–erosion risk of each operating condition. Therefore, a lower score indicates lower corrosion–erosion risk and better overall safety performance.

Table 10. Indicators used for comprehensive safety evaluation of boiler heating surfaces.

Operating Mode	Proportion of Areas with no Corrosion/%	Proportion of Areas with Slight Corrosion/%	Proportion of Areas with Moderate Corrosion/%	Maximum Wear Rate/kg·(m²·s)⁻¹	Average Wear Rate/kg·(m²·s)⁻¹	Sum of Wear Rate/kg·(m²·s)⁻¹
AN	92.73	7.22	0.05	9.11×10^{-6}	9.34×10^{-8}	0.021
AN7CS3-A	87.44	12.34	0.22	1.03×10^{-5}	3.88×10^{-8}	0.019
AN7RS3-A	90.48	8.92	0.60	9.76×10^{-6}	6.52×10^{-8}	0.015
AN7WS3-A	88.96	10.87	0.17	1.14×10^{-5}	9.57×10^{-8}	0.021
AN7CS3-AB	94.12	5.44	0.44	1.75×10^{-5}	8.60×10^{-8}	0.020
AN7RS3-AB	95.23	4.74	0.03	9.34×10^{-6}	3.87×10^{-8}	0.009
AN7WS3-AB	93.74	6.18	0.08	9.04×10^{-6}	7.43×10^{-8}	0.016

4.2. Calculation of Indicator Weights

The entropy value method determines the weight of each indicator by objectively measuring entropy differences between indicators, thereby avoiding the interference of subjective factors. While ensuring objectivity, this method effectively addresses correlations between indicators and possesses high versatility [47,48]. Based on this approach, weight analysis was conducted on the normalized data, and the results are shown in Table 11. The maximum wear rate has the highest weight (28%), followed by the proportion of moderate corrosion and the sum of wear rates, with a weight of 18%. The weights of the

proportion of slight corrosion and the average wear rate are similar (13% and 12%, respectively). The proportion of areas with no corrosion has the smallest weight (8%).

Table 11. Distribution of boiler safety evaluation indicator weights.

Indicator	Entropy	Weight
Proportion of areas with no corrosion	0.87	0.08
Proportion of areas with slight corrosion	0.80	0.13
Proportion of areas with moderate corrosion	0.82	0.18
Maximum wear rate	0.56	0.29
Average wear rate	0.81	0.12
Sum of wear rate	0.71	0.19

4.3. Analysis of Heat Exchange Surface Safety

Based on the weights of each indicator, the comprehensive safety evaluation score for each operating condition was calculated using Equation (10), and the overall scores were determined. The calculated safety scores and rankings of the boiler under seven different operating conditions are presented in Table 12.

$$S_i = \sum_{j=1}^{m} a_j p_{ij} \tag{10}$$

where S_i denotes the comprehensive evaluation value for the *i-th* sample, a_j represents the weight of the *j-th* indicator, and p_{ij} represents the weight of the *i-th* sample under the *j-th* indicator.

Table 12. Boiler safety scores under various operating conditions.

Operating Mode	Comprehensive Evaluation Score	Safety and Stability Ranking
AN	0.46	4
AN7CS3-A	0.42	3
AN7RS3-A	0.48	5
AN7WS3-A	0.60	6
AN7CS3-AB	0.82	7
AN7RS3-AB	0.10	1
AN7WS3-AB	0.32	2

The obtained safety and stability ranking of the boiler under various operating conditions is as follows: AN7RS3-AB > AN7WS3-AB > AN7CS3-A > AN > AN7RS3-A > AN7WS3-A > AN7CS3-AB. In particular, the condition with 30% RS injected from layer AB, mixed with coal, demonstrates superior overall performance in reducing boiler corrosion and wear, offering both environmental and safety advantages. Compared with pure coal combustion, this condition resulted in a 34.3% reduction in the proportion of light corrosion, a 40% reduction in the proportion of moderate corrosion, a 30.2% reduction in the average wear rate, and a 57% reduction in the total wear rate.

5. Conclusions

This study systematically investigated the co-combustion characteristics of coal and biomass, as well as their impacts on boiler safety through integrated theoretical analyses and numerical simulations. Simulations were conducted using the finite volume method based on a 660 MW supercritical tangentially fired coal boiler, and a user-defined function was developed to quantitatively classify high-temperature corrosion levels. In addition,

the erosion behavior was analyzed under various cofiring scenarios. The main conclusions can be summarized as follows:

(1) Under all operating conditions, the H_2S concentration near the furnace wall in the main combustion zone remains elevated, indicating a favorable environment for sulfidic corrosion under reducing-atmosphere conditions. The present CFD assessment focuses exclusively on this sulfidic corrosion mechanism; alkali metal- and chlorine-induced corrosion are not included in the numerical model. Therefore, the results should be interpreted as a sulfidic corrosion-risk assessment rather than a complete prediction of all biomass-related corrosion mechanisms. Biomass injection critically influences the corrosion severity. Compared with pure coal combustion, biomass injection through layer A exacerbates wall corrosion, whereas biomass injection through layer AB effectively mitigates it. In particular, injecting 30% CS via layer A increases the proportion of the wall area subjected to light corrosion by 70.91%. In contrast, injecting RS through layer AB reduces the proportions of light and moderate corrosion degrees by 34.3% and 40.0%, respectively. It is acknowledged that the present CFD model does not dynamically couple ash deposition or slagging effects on wall heat transfer, temperature fields, or flue gas species distributions. These effects may influence local wall heat transfer, temperature fields, and species distributions and should therefore be investigated in future coupled ash-deposition and slagging simulations.

(2) The aerodynamic flow field exhibits a consistent pattern across all conditions, characterized by higher gas velocities near the walls and lower velocities in the furnace center, with a more balanced and reliable overall performance inside the furnace. Erosion is predominantly localized near the burner nozzles. Notably, while biomass cofiring reduces the average erosion rate on the furnace wall by 7.9% (to 30.2%), it concurrently increases the local maximum erosion rate by 7.1% (to 25.1%), localizing wear patterns.

(3) The entropy method was employed to calculate comprehensive evaluation scores for each operating condition, enabling a quantitative performance ranking. The results demonstrate that 30% RS injection via layer AB delivers the most favorable overall performance in simultaneously mitigating boiler corrosion and erosion. Compared with pure coal combustion, this optimal condition achieved a 34.3% reduction in light corrosion, a 40.0% reduction in moderate corrosion, and a 30.2% reduction in the average erosion rate. These findings may provide useful guidance for similar tangentially fired boilers, although further validation is needed before broad generalization.

Author Contributions: Y.T.: Writing—original draft, Software, Methodology, Formal analysis, Data curation. X.X.: Writing—review & editing, Supervision, Resources, Project administration, Conceptualization. L.Z. (Lingjie Zhu): Writing—review & editing, Software, Methodology. L.Z. (Lei Zhang): Validation, Formal analysis. Q.W.: Writing—review & editing, Supervision, Resources. Z.L.: Writing—review & editing, Software. All authors have read and agreed to the published version of the manuscript.

Funding: Financial support for this work was provided by the Science and Technology Program of the Henan Provincial Market Supervision Administration (Grant No. 2023sj49), the Laboratory Work Research Program of Higher Education Institutions in Zhejiang Province (Grant No. YB202572), and the Science and Technology Program of State Administration for Market Regulation (Grant No. 2025MK058).

Data Availability Statement: The plant operating data used in this study are commercially confidential and are therefore not publicly available. The simulation datasets and mesh configurations

generated or analyzed during the current study are available from the corresponding author upon reasonable request, subject to confidentiality restrictions.

Conflicts of Interest: The authors declare that they have no known competing financial interests or personal relationships that could have influenced the work reported in this study.

References

1. Huang, H.; Gao, Y.; Chen, H.;Chen, HA.; Wu, YY.; Wang, JY.; Yu, CL.; Li, JL.; Zou, CW. Biomass briquette fuel, boiler types and pollutant emissions of industrial biomass boiler: A review. *Particuology* **2023**, *77*, 79–90. http://doi.org/10.1016/j.partic.2022.08.016.
2. Awan, M.B.; Iqbal, T.; Yaseen, S.;Nawaz, S.; Ali, C. Techno-economic sustainability analysis of biomass fired industrial boiler: Biomass evolution as heat and power generation source. *Renew. Power Gener. IET* **2019**, *13*, 650–658. http://doi.org/10.1049/iet-rpg.2018.5934.
3. Valente, L.; Tarelho, L.A.C.; Costa, V.A.F. Emissions mitigation by control of biomass feeding in an industrial biomass boiler. *Energy Rep.* **2020**, *6*, 483–489. http://doi.org/10.1016/j.egyr.2019.09.012.
4. Ji, K.; Guo, J.; Bi, X.; Yu, Z.; Si, C.; Hou, S.; Zhou, X.; Dong, X. Effects of low-load operation on biomass boiler performance: Combustion stability, pollutant emission, and boiler efficiency. *Biomass Convers. Biorefinery* **2022**, *15*, 21869–21881. http://doi.org/10.1007/s13399-022-03355-7.
5. Wang, D.; Liu, L.; Yuan, Y.; Yang, H.; Zhou, Y.; Duan, R. Design and key heating power parameters of a newly-developed household biomass briquette heating boiler. *Renew. Energy* **2020**, *147*, 1371–1379. http://doi.org/10.1016/j.renene.2019.09.081.
6. Kobyecki, R.; Zarzycki, R.; Panowski, M.; Winski, M. Numerical analysis of the combustion of straw and wood in a stoker boiler with vibrating grate. *Energy* **2021**, *222*, 119948. http://doi.org/10.1016/j.energy.2021.119948.
7. Gomez, M.A.; Martin, R.; Chapela, S.; Porteiro, J. Steady CFD combustion modeling for biomass boilers: An application to the study of the exhaust gas recirculation performance. *Energy Convers. Manag.* **2019**, *179*, 91–103. http://doi.org/10.1016/j.enconman.2018.10.052.
8. Szlk, A. Effect of Adding Halloysite to Different Solid Biomass Fuels on Combustion Process in a Small-Scale Domestic Retort Boiler. *Energies* **2024**, *17*, 6287. http://doi.org/10.3390/en17246287.
9. Trinh, V.T.; Kim, S.M.; Kim, K.M.; Lee, B.H.; Jeong, T.Y.; Son, J.S.; Kim, J.M.; Jeon, C.H. In-depth numerical analysis of combustion and NOx emission characteristics in a 125 MWe biomass boiler. *Fuel* **2023**, *332*, 125961. http://doi.org/10.1016/j.fuel.2022.125961.
10. Khantisopon, K.; Tharajak, J.; Nawarat, P.; Sanpo, K.; Ang, A. High-temperature corrosion investigations of deposit containing eutectic KCl-K_2SO_4 mixture on AISI 1015 and SS304 steels. *Corros. Sci. J. Environ. Degrad. Mater. Its Control* **2022**, *205*, 110470. http://doi.org/10.1016/j.corsci.2022.110470.
11. Ruozzi, A.; Vainio, E.; Kinnunen, H.; Hupa, L. Cold-end corrosion in biomass combustion–Role of calcium chloride in the deposit. *Fuel* **2023**, *349*, 11. http://doi.org/10.1016/j.fuel.2023.128344.
12. Magdziarz, A.; Gajek, M.; Nowak-Wozny, D.; Wilk, M. Mineral phase transformation of biomass ashes–Experimental and thermochemical calculations. *Renew. Energy* **2018**, *128*, 446–459. http://doi.org/10.1016/j.renene.2017.05.057.
13. Wu, D.; Yuan, Z.; Liu, S.;Zheng, J.; Wei, X.; Zhang, C. Recent Development of Corrosion Factors and Coating Applications in Biomass Firing Plants. *Coatings* **2020**, *10*, 1001. http://doi.org/10.3390/coatings10101001.
14. Paz, M.; Zhao, D.; Karlsson, S.; Liske, J.; Jonsson, T. Investigating corrosion memory: The influence of previous boiler operation on current corrosion rate. *Fuel Process. Technol.* **2017**, *156*, 348–356. http://doi.org/10.1016/j.fuproc.2016.09.018.
15. Vlček, J.; Ovčačíková, H.; Velička, M.; Topinková, M.; Burda, J.; Matejková, P. The corrosion effect of fly ash from biomass combustion on andalusite refractory materials. *Minerals* **2023**, *13*, 357. http://doi.org/10.3390/min13030357.
16. Wang, L.; Ma, Z.R.; Zhao, C.L.; Zhou, J.; Wang, H.; Li, G.; Zhou, N. New problems of boiler corrosion after coupling combustion of coal and biomass and anti-corrosion technologies. *J. Renew. Mater.* **2024**, *12*, 799–814. http://doi.org/10.32604/jrm.2024.047343.
17. Yuan, M.B.; Deng, L.; Zhang, J.K.; Jiang, J.H.; Liang, Y.; Liu, H.; Che, D.F. Prediction of H_2S corrosion depth for water-cooled wall in lower furnace of utility boiler. *Fuel* **2022**, *329*, 125466. http://doi.org/10.1016/j.fuel.2022.125466.
18. Cao, L.T.; Peng, R.; Deng, Z.Y. Optimization study on high-temperature corrosion prevention of the water wall of a 1000MW dual circle tangential boiler during operation. *Energy Rep.* **2021**, *7*, 915–925. http://doi.org/10.1016/j.egyr.2021.09.181.

19. Grochowalski, J.; Widuch, A.; Sadek, S.; Melka, B.; Nowak, M.; Klimanek, A.; Andrzejczyk, M.; Klajny, M.; Czarnowska, L.; Hernik, B.; et al. Technique for reducing erosion in large-scale circulating fluidized bed units. *Powder Technol.* **2023**, *426*, 118651. http://doi.org/10.1016/j.powtec.2023.118651.
20. Yoneda, S.; Hayashi, S.; Miyakoshi, Y.; Kogin, T.; Ishikawa, E.; Noguchi, M. Erosion-Corrosion Behavior of Ni-20Cr-4Fe and Ni-20Cr-4Fe-7Mo under Fluidized-Bed Biomass Boiler Conditions. *Corros. Sci.* **2022**, *205*, 110472. http://doi.org/10.1016/j.corsci.2022.110472.
21. Bhosale, D.G.; Prabhu, T.R.; Rathod, W.S.; Patil, M.A.; Rukhande, S.W. High temperature solid particle erosion behaviour of SS 316L and thermal sprayed WC-Cr_3C_2–Ni coatings. *Wear* **2020**, *462–463*, 203520. http://doi.org/10.1016/j.wear.2020.203520.
22. Vinod, K.M.; Suresh, R.; Jegadeeswaran, N. Study of solid particle erosion behavior of HVOF spray coated superco-605 super-alloy. *Mater. Today Proc.* **2021**, *45*, 10–14. http://doi.org/10.1016/j.matpr.2020.09.103.
23. Orumbayev, R.K.; Bakhtiyar, B.T.; Umyshev, D.R.; Kumargazina, M.B.; Otynchiyeva, M.T.; Akimbek, G.A. Experimental study of ash wear of heat exchange surfaces of the boiler. *Energy* **2021**, *215*, 119119. http://doi.org/10.1016/j.energy.2020.119119.
24. Wu, W.Y.; Wei, B.; Li, G.H.; Chen, L.J.; Wang, J.J.; Ma, J.R. Study on ammonia gas high temperature corrosion coupled erosion wear characteristics of circulating fluidized bed boiler. *Eng. Fail. Anal.* **2022**, *132*, 105896. http://doi.org/10.1016/j.engfailanal.2021.105896.
25. Saarivirta, E.H.; Kinnunen, H.; Tuiremo, J.; Uusitalo, M.; Antonov, M. Erosive wear of boiler steels by sand and ash. *Wear* **2014**, *317*, 213–224. http://doi.org/10.1016/j.wear.2014.06.007.
26. Kobyecki, R.; Zarzycki, R.; Panowski, M.; et al. Numerical analysis of the combustion of straw and wood in a stoker boiler with vibrating grate. *Energy* **2021**, *222*, 119948. http://doi.org/10.1016/j.energy.2021.119948.
27. Du, J.; Yang, J.; Zhao, Y.; Guo, Q.; Da, Y.; Che, D. Numerical study on effect of flue gas recirculation and co-firing with biomass on combustion characteristics in octagonal tangentially lignite-fired boiler. *Energies* **2024**, *17*, 475. http://doi.org/10.3390/en17020475.
28. Varapiang, T.; Rangton, N.; Nukkhong, W.; Nukkhong, W.; Wises, P.; Piumsomboon, P.; Piemjaiswang, R.; Chalermsinsuwan, B. Digital twin of biomass/coal co-firing circulating fluidized bed boiler by using computational fluid dynamics simulation. *Energy Rep.* **2023**, *9*, 6–9. http://doi.org/10.1016/j.egyr.2023.09.110.
29. Zhang, H.D.; Li, W.B.; Ma, Q.;. Zhang, Y.W.; Lei, F.L. Numerical study on influence of exit geometry in gas–solid flow hydrodynamics of HDCFB riser by CPFD. *Adv. Powder Technol.* **2020**, *31*, 4005–4017. http://doi.org/10.1016/j.apt.2020.08.006.
30. Zhang, Z.; Chen, D.; Li, Z.; Cai, N.; Imada, J. Development of Sulfur Release and Reaction Model for CFD Modeling in Sub-bituminous Coal Combustion. *Energy Fuels* **2017**, *31*, 1383–1398. http://doi.org/10.1021/acs.energyfuels.6b02867.
31. Sivasankaran, S.; Bhuvaneswari, M.; Amer, A.A. Numerical study on buoyant convection and thermal radiation in a cavity with various thermal sources and Cattaneo-Christov heat flux. *Case Stud. Therm. Eng.* **2021**, *27*, 101207. http://doi.org/10.1016/j.csite.2021.101207.
32. Miller, J.A.; Bowman, C.T. Mechanism and modeling of nitrogen chemistry in combustion. *Prog. Energy Combust. Sci.* **1989**, *15*, 287–338. http://doi.org/10.1016/0360-1285(89)90017-8.
33. Chen, S.; Zhao, W.; Fan, Y.; Wang, X.; Guan, X.; Guo, Z.; Yan, Y.; Zhang, Z.; Li, L. Synergistic corrosion mechanism of boiler steel by SO_2-Cl_2-O_2 at extreme 800 °C during copper smelting. *Eng. Fail. Anal.* **2025**, *169*, 109204. http://doi.org/10.1016/j.engfailanal.2024.109204.
34. Hardy, T.; Kakietek, S.; Halawa, K.; Moscicki, K.; Janda, T. Determination of High Temperature Corrosion Rates of Steam Boiler Evaporators Using Continuous Measurements of Flue Gas Composition and Neural Networks. *Energies* **2020**, *13*, 3134. http://doi.org/10.3390/en13123134.
35. Mirzaei, M.; Clausen, S.; Wu, H.; Nakhaei, M.; Zhou, H.; Jonck, K.; Jensen, P.; Lin, W. Investigation of erosion in an industrial cyclone preheater by CFD simulations. *Powder Technol.* **2023**, *421*, 118424. http://doi.org/10.1016/j.powtec.2023.118424.
36. Mu, L.; He, S.; Chen, S.; Chen, X.; Shi, J.; Zhang, Y.; Liu, C. Prediction of bend-pipeline erosion field based on CFD and reduced order method. *Chem. Eng. Process. -Process Intensif.* **2025**, *213*, 110320. http://doi.org/10.1016/j.cep.2025.110320.
37. Bian, C.; Huang, J.; Sun, R. Numerical optimization of combustion and NO_x emission in a retrofitted 600MWe tangentially-fired boiler using lignite. *Appl. Therm. Eng.* **2023**, *226*, 120228. http://doi.org/10.1016/j.applthermaleng.2023.120228.
38. Zhu, B.; Shang, B.; Guo, X.Z.L. Study on Combustion Characteristics and NOx Formation in 600 MW Coal-Fired Boiler Based on Numerical Simulation. *Energies* **2023**, *16*, 262. http://doi.org/10.3390/en16010262.
39. Du, Z.; Liu, L.; Li, M.; Zhang, X.; Li, Y.; Hao, M.; Gao, J.; Ren, X. Numerical Simulation of Co-Firing Biomass in a 660 MW Coal-Fired Boiler. *Energies* **2025**, *18*, 6082. http://doi.org/10.3390/en18236082.

40. Wang, H.; Jin, H.; Yang, Z.; Deng, S.; Wu, X.; An, J.; Sheng, R.; Ti, S. CFD modeling of flow, combustion and NOx emission in a wall-fired boiler at different low-load operating conditions. *Appl. Therm. Eng.* **2024**, *236*, 121824. http://doi.org/10.1016/j.applthermaleng.2023.121824.
41. Zhu, L.; Xu, X.; Wang, Q.; Wang, H.; Feng, J.; Zhang, L. Development of a comprehensive model for evaluating slagging characteristics in the Co-combustion of coal and biomass. *J. Energy Inst.* **2025**, *118*, 101927. http://doi.org/10.1016/j.joei.2024.101927.
42. Niu, Y.; Tan, H.; Hui, S. Ash-related issues during biomass combustion: Alkali-induced slagging, silicate melt-induced slagging (ash fusion), agglomeration, corrosion, ash utilization, and related countermeasures. *Prog. Energy Combust.* **2016**, *52*, 1–61. http://doi.org/10.1016/j.pecs.2015.09.003.
43. Chen, S.; He, B.; He, D.; Cao, Y.; Ding, G.; Liu, X.; Duan, Z.; Zhang, X.; Song, J.; Li, X. Numerical investigations on different tangential arrangements of burners for a 600 MW utility boiler. *Energy* **2017**, *122*, 287–300. http://doi.org/10.1016/j.energy.2017.01.093.
44. Mousavi, S.M.; Fatehi, H.; Bai, X.S. Numerical study of the combustion and application of SNCR for NOx reduction in a lab-scale biomass boiler. *Fuel* **2021**, *293*, 120154. http://doi.org/10.1016/j.fuel.2021.120154.
45. Yan, J.; Li, J.; Jin, D.; Liu, X.; Zhang, W.; Wang, H. Numerical investigation of boiler waterwall corrosion by integrated tube temperature prediction and sulfur evolution model. *Numer. Heat Transf. Part A Appl.* **2025**, *86*, 3432–3451. http://doi.org/10.1080/10407782.2023.2301046.
46. Kim, Y.S.; Kim, M.K.; Fu, N.; Fu, N.; Liu, J.Y.; Wang J.Q.; Srebric, J. Investigating the impact of data normalization methods on predicting electricity consumption in a building using different artificial neural network models. *Sustain. Cities Soc.* **2025**, *118*, 105570. http://doi.org/10.1016/j.scs.2024.105570.
47. Chen, C.H.; Zhang, H.J. Evaluation of green development level of mianyang agriculture, based on the entropy weight method. *Sustainability* **2023**, *15*, 7589. http://doi.org/10.3390/su15097589.
48. Yuan, W.; Liu, Z. Study on evaluation method of energy-saving potential of green buildings based on entropy weight method. *Int. J. Glob. Energy Issues* **2023**, *45*, 448–460. http://doi.org/10.1504/ijgei.2023.132014.

Disclaimer/Publisher's Note: The statements, opinions and data contained in all publications are solely those of the individual author(s) and contributor(s) and not of MDPI and/or the editor(s). MDPI and/or the editor(s) disclaim responsibility for any injury to people or property resulting from any ideas, methods, instructions or products referred to in the content.